ACS OMEGA

http://pubs.acs.org/journal/acsodf

Article

Scalable Advanced $Li(Ni_{0.8}Co_{0.1}Mn_{0.1})O_2$ Cathode Materials from a Slug Flow Continuous Process

Mingyao Mou, Arjun Patel, Sourav Mallick, Bishnu P. Thapaliya, Mariappan Parans Paranthaman,* Jethrine H. Mugumya, Michael L. Rasche, Ram B. Gupta, Selma Saleh, Sophie Kothe, Ena Baral, Gaind P. Pandey, Herman Lopez, and Mo Jiang*

Cite This: *ACS Omega* 2022, 7, 42408−42417

Read Online

ACCESS | Metrics & More | Article Recommendations | Supporting Information

ABSTRACT: $Li[Ni_{0.8}Co_{0.1}Mn_{0.1}]O_2$ (LNCMO811) is the most studied cathode material for next-generation lithium-ion batteries with high energy density. However, available synthesis methods are time-consuming and complex, restricting their mass production. A scalable manufacturing process for producing NCM811 hydroxide precursors is vital for commercialization of the material. In this work, a three-phase slug flow reactor, which has been demonstrated for its ease of scale-up, better synthetic control, and excellent uniform mixing, was developed to control the initial stage of the coprecipitation of NCM811 hydroxide. Furthermore, an equilibrium model was established to predict the yield and composition of the final product. The homogeneous slurry from the slug flow system was obtained and then transferred into a ripening vessel for the necessary ripening process. Finally, the lithium−nickel−cobalt−manganese oxide was obtained through the calcination of the slug flow-derived precursor with lithium hydroxide, having a tap density of 1.3 g cm^{-3} with a well-layered structure. As-synthesized LNCMO811 shows a high specific capacity of 169.5 mAh g^{-1} at a current rate of 0.1C and a long cycling stability of 1000 cycling with good capacity retention. This demonstration provides a pathway toward scaling up the cathode synthesis process for large-scale battery applications.

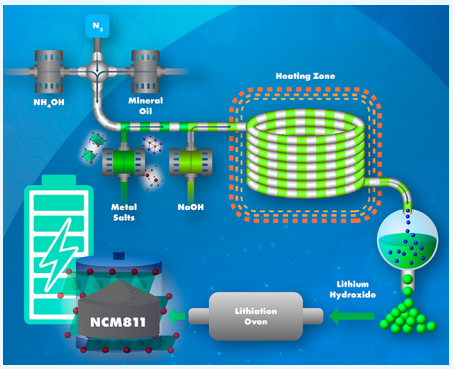

1. INTRODUCTION

The expanding demands for lithium-ion batteries (LIBs) in portable electronic devices (e.g., smartphones, tablet PCs) and environmental-friendly vehicles (e.g., electric and/or hybrid vehicles) require researchers to further improve safety, extend battery life, increase charge capacity, and reduce cost.[1−11] One of the most advanced material options is the layered nickel-rich $LiNi_xCo_yMn_zO_2$ cathode.[12−15] The cathode material is one of the key cost drivers in lithium-ion batteries. The typical cost of an nickel-cobalt-manganese oxide (NCM) material is $25/kg, or $2,151/pack, or $160/$KWh_{Useable}$.[5] Among the various Ni-rich NCMs, the layered NCM811 is advantageous in terms of theoretical capacity (~200 mAh g^{-1}) as well as the actual specific capacity.[16] However, during the continuous charge−discharge cycling, the transformation of Ni^{4+} into the lower valent nickel oxides causes an abrupt phase change from layered to rocksalt structure.[16,17] The change in crystal structure facilitates the consumption of exposed active Li^+ by electrolyte leading to the formation of cathode electrolyte interface (CEI), resulting in the reduction of discharge capacity of the active material.[16] Besides this, the corrosion of cathode material by HF, cation mixing, and the formation of an inert layer of Li_2CO_3/LiOH on the surface of active material are a few of the standing issues with the layered NCM811, which are required to be addressed.[18−22] Various modification techniques, including coating, doping, morphology design, and regulating the crystal structure, are already reported in the literature to overcome the aforementioned limitations.[23−25]

Large-scale and cost-effective production of battery cathode materials, specifically high-Ni-content NCM-based materials without compromising the battery performance, are needed. There are many synthesis methods[26] developed for these NCM materials, including coprecipitation, spray drying/pyrolysis,[26,27] solid-state method, sol−gel synthesis,[28] and combustion method.[29] Most of the methods are not suitable for bulk-scale production of high-Ni-content NCMs with specific elemental compositions due to poor control over reaction steps as well as poor reproducibility. Solid-state-based methods are straightforward, but the coprecipitation method provides much more uniform mixing, with better product control and simpler equipment needs, thus being popular in industries and applied to complex particles. For scaling-up production, most batch processes require additional experi-

Received: August 26, 2022
Accepted: October 26, 2022
Published: November 8, 2022

ments and troubleshooting in larger-scale equipment (e.g., larger diameter reactor) to control or maintain the same product specifications.[30−34]

To overcome the scale-up problem between lab scale and industrial scale, various continuous manufacturing processes have been successfully developed in the petroleum,[35] food,[36] and pharmaceutical industries.[37−39] Therefore, we evaluated a scalable continuous synthesis process for preparing high-quality battery precursors. Tubular slug flow reactors are one kind of continuous reactor that has advantages including good internal mixing, better synthetic control, easy scale-up, etc.[40,41] To achieve better control over the reagent addition process, a three-phase slug flow reactor was chosen to realize the continuous synthesis of battery precursor materials.[42] In this case, the identical liquid slugs or segments are separated by the gas phase and both the aqueous and gas phases are isolated by the oil phase from the tubing wall, which further prevents fouling and clogging. Meanwhile, it can facilitate the uninterrupted production of the material with high phase purity. The slug flow does not change the reaction parameters (reaction type, reactant choice, reactant concentration) compared with the traditional batch reactor, and each slug acts as an independent functional reactor of a microliter scale volume with excellent internal mixing and enhanced heat and mass transfer.[40] In this way, useful operational properties of both batch (e.g., no clogging) and continuous crystallizers (e.g., control of the process and product quality and the ease of scale-up[43]) are obtained in a continuous flow reactor. The scale-up process of a slug flow reactor can be achieved by simply running the experiment for a longer time to generate more slugs.

Here, we designed a multistep slug flow process to realize the continuous coprecipitation process. Drawbacks like hotspots and mass/concentration gradients commonly occurred in batch reactors and are not observed in slug flow reactors. Therefore, the precipitation process and product quality were improved in the slug flow reactors. An equilibrium model was also developed to predict the yield and composition at various pH values. The lithiated NCM811 hydroxide-based LIB coin cell shows a specific capacity of 169.5 mAh g^{-1} at a current rate of 0.1C and retains up to 128.77 mAh g^{-1} at 1C. The Li^+ diffusion coefficient is calculated from the impedance analysis, and the magnitude is on the order of 10^{-11}, which follows a similar trend with the already reported high-Ni-content NCMs.[1,44]

2. EXPERIMENTAL PROCEDURE

2.1. Materials. Ammonium hydroxide (28% NH_3 in H_2O, purity ≥99.99%), nickel(ii) sulfate hexahydrate (≥98%), cobalt(ii) sulfate heptahydrate (≥99%), manganese(ii) sulfate monohydrate (≥99%), light mineral oil, and lithium hydroxide (≥98%) were purchased from Sigma-Aldrich. Sodium hydroxide (≥98%) was purchased from J.T. Baker. All of the solutions were prepared in deionized water. All chemicals were used with no further treatments.

2.2. Slug Flow Synthesis of NCM811 Hydroxide Precursor. A more common two-phase liquid/gas slug flow reactor was developed first for the slug flow process. However, serious fouling occurred due to the fast precipitation process, which finally leads to clogging and uncontrolled chemical reaction. Therefore, a fouling-free three-phase slug flow reactor (3PSFR) was designed for the continuous coprecipitation process (detailed in Section 3.1). Generally, a 0.5 M metal ion solution (consisting of nickel−cobalt−manganese sulfates with a molar ratio of 8:1:1) with a flow rate of 1.5 mL min^{-1} was added to 2 M NH_4OH solution at a flow rate of 0.9 mL min^{-1}. And then, a 2 M NaOH aqueous solution was pumped into the slurry slug with a flow rate of 1.3 mL min^{-1}. The residence time within the slug flow reactor is set at 6 min. The precursors produced by 3PSFR were ripened for 15 h in a batch reactor, and the product was then washed, filtered, and dried.

2.3. Lithiation of the Precursor Materials. $LiNi_{0.8}Co_{0.1}Mn_{0.1}O_2$ (LNCMO811) was prepared by mixing the corresponding hydroxide precursors with stoichiometric quantities of LiOH in a mortar and pestle for 10 min. The ground samples were then calcined at a rate of 3 °C min^{-1} in oxygen from room temperature to 770 °C and held at 770 °C for 10 h followed by furnace cooling.

2.4. Material Characterizations. The morphology of the primary and secondary particles of the precursor and lithiated samples was analyzed using scanning electron microscopy (SEM, Hitachi SU-70 FE-SEM). The phase contents of the precursor and lithiated samples were determined using X-ray diffraction (XRD, Empyrean multipurpose X-ray diffractometer) with a Cu Kα radiation source and a wavelength of 1.5406 Å. Tap density was measured using Auto tap from Quantachrome instruments. The chemical composition of the samples was measured using inductively coupled plasma-optical emission-mass spectrometry (ICP-OES, Agilent Technologies, 5110-MS). Differential scanning calorimetry (DSC) and thermogravimetry (TGA) were measured using a DSC Q1000 and TGA Q500 at a temperature ramp of 10 °C/min from the TA instrument, respectively.

2.5. Electrochemical Measurements. The cathode slurry was prepared by uniformly mixing the active materials (NCM811), carbon black as the conductive agent and poly(vinylidene difluoride) (PVDF) as the binder in N-methyl pyrrolidone (NMP) solvent in a weight ratio of 8:1:1. The cathode was prepared by casting the slurry onto a battery-grade aluminum foil using the doctor blade technique followed by drying at 130 °C for 12 h under vacuum. Then, the cathode-coated foil was calendared and cut to the required diameter of 15 mm. The loading of the active material on the cathode was 4.017 mg cm^{-2}, and the calendaring thickness was 0.21 cm. The coin cells were fabricated using the NCM811-based cathode, lithium metal as the anode, and the electrolyte-soaked Celgard 2340 trilayer microporous membrane as the separator. 1 M $LiPF_6$ in ethylene carbonate/dimethyl carbonate (EC/DMC = 50/50 (v/v)) was used as the electrolyte. The batteries were assembled inside an argon-filled glovebox. In the case of performing the electrochemical experiments, 1C = 200 mAh g^{-1} was considered and electrochemical impedance spectroscopy (EIS) was performed. Cyclic voltammetry and charge/discharge experiments were carried out in an MTI battery cycler. EIS was performed after five discharge−charge cycles with an amplitude of 5 mV at a frequency range of 100 kHz to 10 MHz using a Gamry potentiostat Interface 5000E. All electrochemical tests were conducted at room temperature.

2.6. Theoretical Calculations for the Yield. In an attempt to understand the effect of ammonia concentration and pH on the yield of the precursor material, a synthesis model was developed. An NCM811 hydroxide batch synthesis model was developed from aqueous equilibrium constants (see Table S2) using mass action expressions and overall mass balances.[45,46] The overall concentration of ammonia $[NH_3]_T$ and metals in solution $[M_j]_T$ can be expressed as

https://doi.org/10.1021/acsomega.2c05521
ACS Omega 2022, 7, 42408−42417

$$[NH_3]_T = [NH_3] + [NH_4^+] + \sum_{j=1}^{3}\sum_{i=1}^{6} i[M_j(NH_3)_i^{2+}] \quad (1)$$

$$[M_j]_T = [M_j^{2+}] + \sum_{j=1}^{6}[M_j(NH_3)_i^{2+}] + \sum_{i=1}^{4}[M_j(OH)_i^{(2-i)+}],\ j = 1, 2, 3 \quad (2)$$

where the index j = 1, 2, or 3 corresponds to nickel, cobalt, or manganese, respectively, and the values of the index, i, in the summations over metal amine and metal hydroxide complexes are limited to the complexes for which equilibrium constants are listed in Table S3.

At equilibrium, substitution using the mass action expressions allows for eqs 1 and 2 to be written as

$$[NH_3]_T = [NH_3] + \frac{K_A[NH_3]}{[OH^-]} + \sum_{j=1}^{3}\sum_{i=1}^{6} iK_{MA,ji}[M_j^{2+}][NH_3]^i \quad (3)$$

$$[M_j]_T = [M_j^{2+}]\left\{1 + \sum_{i=1}^{6} K_{MA,ji}[NH_3]^i + \sum_{i=1}^{4} K_{MOH,ji}[OH^-]^i\right\},\ j = 1, 2, 3 \quad (4)$$

The equilibrium constants denoted $K_{MA,ji}$ correspond to the metal amine complexes with metal j in association with i ammonia molecules. Similarly, the $K_{MOH,ji}$ corresponds to metal j in complex with i hydroxide ions. Recognition that the equilibrium expressions for water and the solubility products allow for the following additional expressions

$$[OH^-] = \frac{K_w}{[H^+]} = K_w 10^{pH} \quad (5)$$

$$[M_j^{2+}] = \frac{K_{spMOH,j}}{[OH^-]^2} = \frac{K_{spMOH,j}}{(K_w 10^{pH})^2} \quad (6)$$

elucidating that the total concentrations of the transition metals, $[M_j]_T$, in solution at equilibrium are determined by the total ammonia concentration, $[NH_3]_T$, in solution and the pH; any metals in excess will necessarily precipitate, given sufficient time. While secondary particle formation occurs over a period of hours in a ripening vessel downstream of the slug flow reactor, nucleation and growth of primary particles occur rapidly within the slugs of the slug flow reactor and account for most of the overall desaturation, as seen in experiments. Therefore, without consideration of the particle size distribution or morphology, the theoretical maximum yield of the slug flow reactor is fully determined by the equilibrium calculation using the total ammonia concentration of a slug and the pH measured at the outlet of the slug flow reactor (as shown in Figure 1).

For the experimental conditions described in Section 3.1, the total ammonia concentration within a slug can be approximated as 0.5 M. The pH measured at the exit of the slug flow reactor is approximately 10. From Figure 1, the maximum yield before ripening is 75%. The composition of metals within the precipitate at the 0.5 M total ammonia concentration can be found as a function of pH (Figure 2).

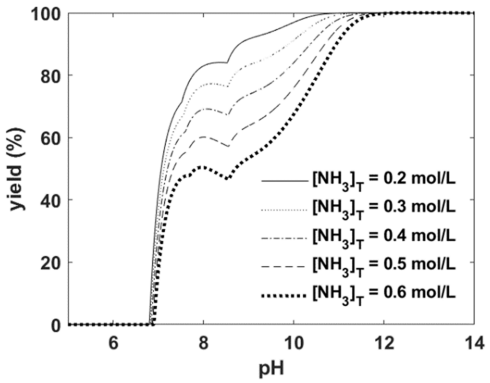

Figure 1. Maximum yield of the slug flow reactor is specified by the total ammonia concentration and the exit pH.

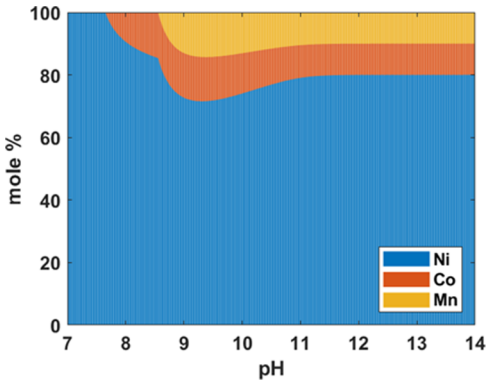

Figure 2. Composition of metals within the hydroxide precipitate as a function of pH when the total ammonia concentration is 0.5 M.

At pH = 10, the composition of the NCM hydroxide precipitate at the exit of the slug flow reactor predicted by the model is 74:13:13% with respect to the nickel−cobalt−manganese components. The yield and composition predicted by the model would hold if the system were allowed to reach equilibrium at a pH of 10 with no loss of ammonia due to evaporation. The limitations of this equilibrium model also include ignorance of the exact relative rates at which each metal reaches equilibrium among its corresponding complexes and hydroxide precipitates.

3. RESULTS AND DISCUSSION

3.1. Three-Phase Slug Flow Process Design. The slug flow process and parameters are modified based on the batch coprecipitation process reported in the literature.[46,47] Typically, the transitional-metal ion solution reacts with chelating reagents $NH_3{\cdot}H_2O$ and NaOH at pH 11.5 and a temperature of 60 °C. A three-phase liquid/liquid/gas slug flow reactor was designed to synthesize the NCM hydroxide precursor based on the procedure (Figure 3) described. The ammonium hydroxide (2 M), mineral oil, and nitrogen streams formed a three-phase slug flow via the cross-junction. Liquids were fed using syringe pumps (SyringeOne, New Era Inc.), and nitrogen flow was controlled by a mass flow controller (FMA-2617A, Omega Engineering). The 0.5 M metal ion solution (nickel−cobalt−

https://doi.org/10.1021/acsomega.2c05521
ACS Omega 2022, 7, 42408−42417

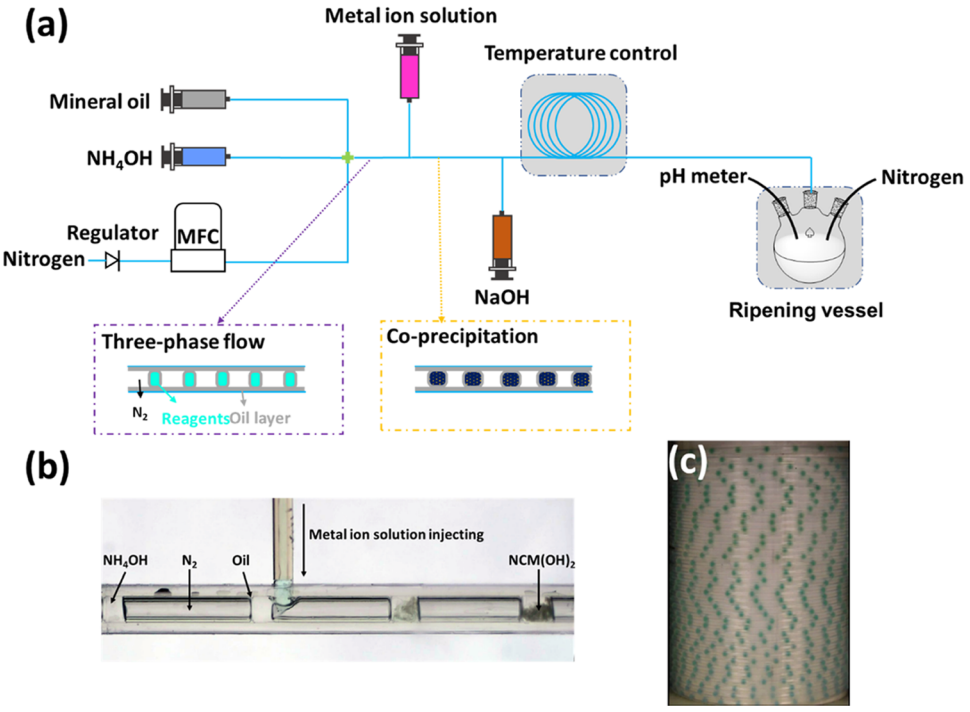

Figure 3. (a) Illustration of the designed three-phase slug flow reactor to produce the NCM811 hydroxide precursor; (b) continuous coprecipitation process achieved via a house-built Tee connector; and (c) three-phase slug flow reactor.

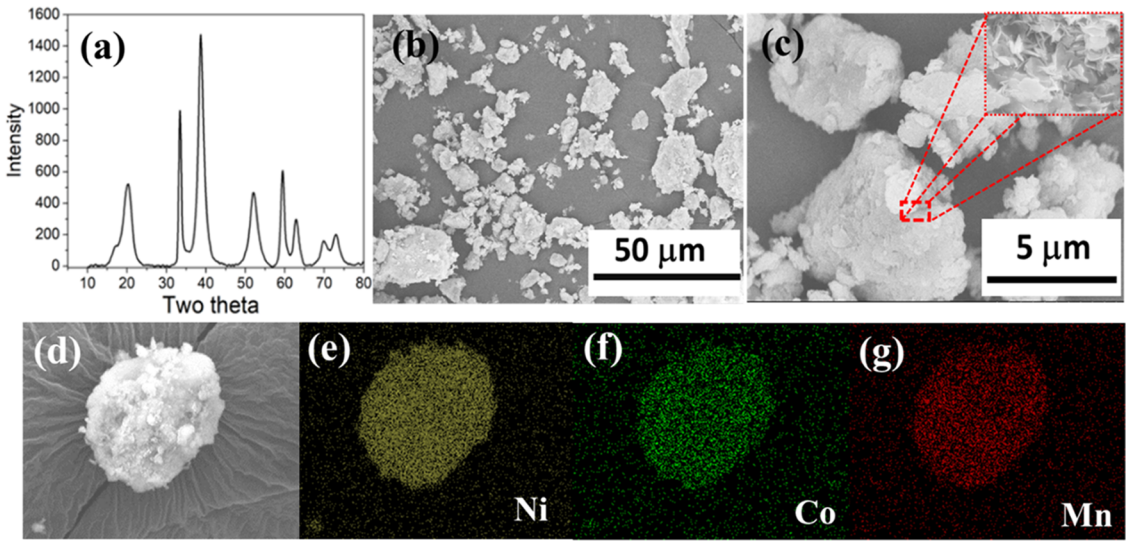

Figure 4. Characterization of the precursor $[Ni_{0.8}Co_{0.1}Mn_{0.1}](OH)_2$. (a) XRD pattern, (b, c) SEM images, and (d–g) elemental mapping.

manganese sulfates with a molar ratio of 8:1:1) was injected into the moving three-phase stream via a house-built Tee connector. The concentration of the metal ion solutions was diluted to maintain low viscosity and good mixing inside the slugs/microreactors. The inner diameter of the tubing is 2.4 mm (FEP Plastic, McMaster-Carr), and the residence time inside the 3PSFR was around 6 min. Volumetric flow rates of each stream are set at Q_{oil} = 0.8 mL min^{-1}, Q_{N_2} = 25 SCCM, Q_{NH_4OH} = 0.9 mL min^{-1}, Q_{metal} = 1.5 mL min^{-1}, and Q_{NaOH} = 1.3 mL min^{-1}. Temperature is controlled at 60 °C for both the slug flow reactor (Figure 3c) and the ripening flask. As can be seen in Figure 3b, precipitation was initiated right after the injection of NCM811 solution into the NH_4OH droplet. Then, the NaOH (2 M) was introduced into the well-mixed slugs to increase the pH to 11.5. Within the continuous reactor, the precipitation process was the same for every slug/droplet passing by a fixed point such as the Tee-mixer in Figure 3b. It is worth noting that in a batch reactor, the precipitation process is difficult to control. The small volume of each slug/microreactor (typical size is 10–40 μL) and good mixing can achieve better precipitation control. All of the slugs shared identical attributes including volume, temperature, heat and mass transfer, and kinetics.[48] The scale-up process can be carried out by simply operating the pumps for a longer time. The scale-up process does not change the actual reactor size (i.e., the volume of the slugs) or the microenvironment that each slug experienced; hence, the same product quality can be obtained. After the initial coprecipitation process was

https://doi.org/10.1021/acsomega.2c05521
ACS Omega 2022, 7, 42408–42417

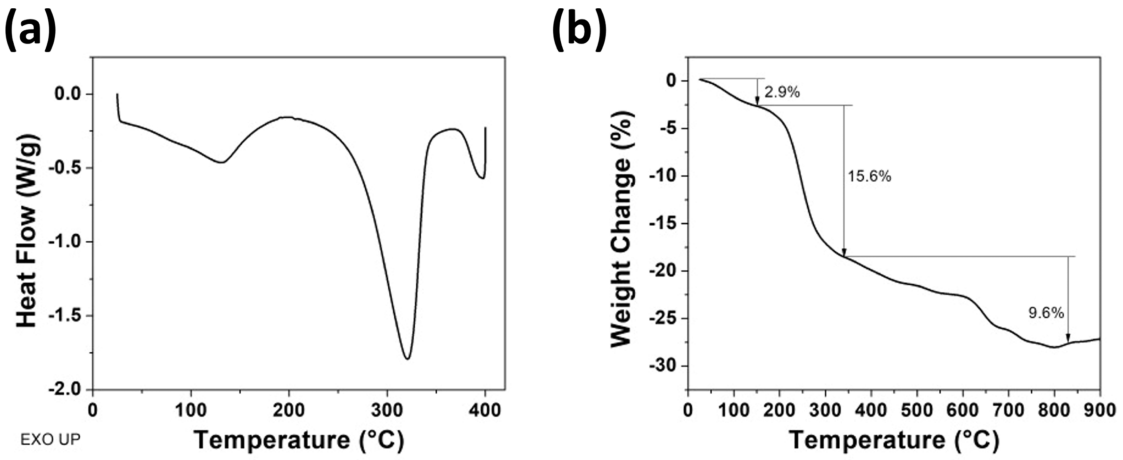

Figure 5. (a) TGA and (b) DSC profile of the slug flow-synthesized NCM811 hydroxide precursor.

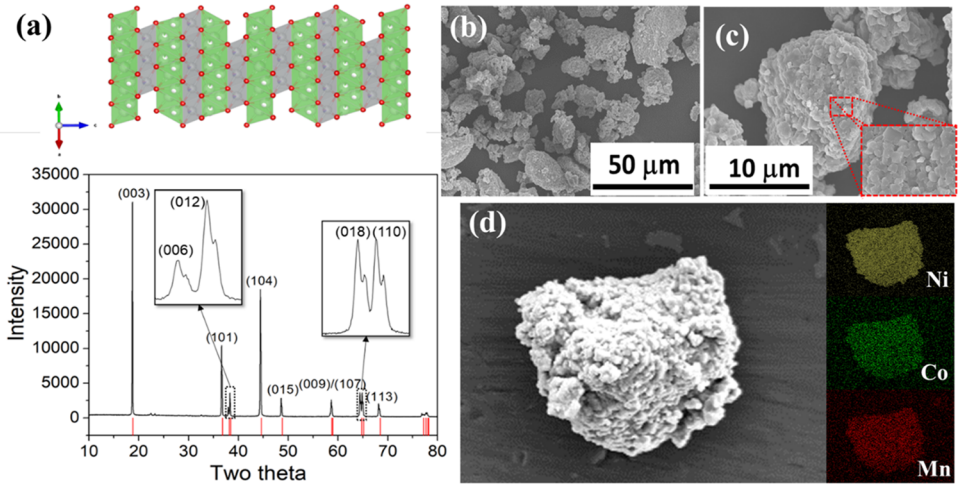

Figure 6. Characterization of the cathode material LNCMO811. (a) XRD pattern. Red lines are reference spectra from ICDD#04-023-5128, with the structural model presented above the spectra; (b, c) SEM images; and (d) elemental mapping.

completed in the continuous slug flow reactor, the slurry slug was collected in a batch reactor for ripening and the ripening time was 15 h. An inert atmosphere was required for the ripening flask to prevent oxidation. Impurity peaks were observed when the ripening flask was open to the air (Figure S1). The slurry (brownish) was centrifuged, washed, and dried at 60 °C. Mineral oil can be recycled.

3.2. Solid-State Characterization of the Materials. All of the XRD (Figure 4a) characteristic peaks match well with the reported patterns.[46,49] Figure 4b shows SEM images of the as-synthesized NCM811 hydroxide precursor displayed nanosheet morphology for the primary particles. No specific secondary particle shape has been observed. The ideal atomic ratio of Ni/Co/Mn should match the feeding number. However, Mn-deficiency is usually observed due to the high solubility of Mn compared to the other two transitional metals.[50] ICP-OES analysis yielded an atomic ratio of Ni 81%, Co 10%, and Mn 9%, indicating a negligible Mn-deficiency for the as-synthesized NCM hydroxide. Energy dispersive X-ray (EDX) mapping (Figure 4d−g) indicated that the Ni, Co, and Mn were evenly distributed within the precursor particles. TGA (Figure 5) results show that the first-stage weight loss was observed under 100 °C, indicating the presence of absorbed surface water. Weight loss of 15.6% was observed from the temperature range of around 120−340 °C. This provides an estimate that the as-synthesized NCM811 precursor possesses one structural water molecule from calculating the theoretical weight loss value of $Ni_{0.8}Co_{0.1}Mn_{0.1}OH{\cdot}H_2O$ (16.3%). The decomposition of $Ni_{0.8}Co_{0.1}Mn_{0.1}OH$ started at around 340 °C and was completed at around 800 °C, along with obtaining $Ni_{0.8}Co_{0.1}Mn_{0.1}O$ and releasing water.[51] Three endothermic peaks in the DSC spectra confirm the three processes observed in TGA: surface water loss around 100 °C, bind water loss around 200−340 °C, and decomposition above 350 °C.

$$\text{dehydration: } Ni_{0.8}Co_{0.1}Mn_{0.1}(OH)_2{\cdot}H_2O \rightarrow Ni_{0.8}Co_{0.1}Mn_{0.1}(OH)_2 + H_2O \quad (7)$$

$$\text{decomposition: } Ni_{0.8}Co_{0.1}Mn_{0.1}(OH)_2 \rightarrow Ni_{0.8}Co_{0.1}Mn_{0.1}O + H_2O \quad (8)$$

The synthesized hydroxide precursor was calcinated and lithiated. XRD spectra of the lithiated sample show the same diffraction patterns of LNCMO (ICDD#04-023-5128), which belongs to the $\bar{R}3m$ group. The distinct splitting of (006)/(012) and (018)/(110) indicates the formation of a well-

https://doi.org/10.1021/acsomega.2c05521
ACS Omega 2022, 7, 42408−42417

ordered layered structure and high crystallinity (Figure 6a). The large c/a value in Table 1 also indicated a well-ordered layered structure.[52] The intensity ratio of (003) and (104) is an indicator of the degree of cation mixing. Higher $I_{(003)}/I_{(104)}$ indicates a lower degree of cation mixing in the sample. In this paper, we report the $I_{(003)}/I_{(104)}$ ratio to be 1.7, indicating that the product prepared has a low degree of cation mixing than normally reported (usually between 1.4 and 1.6).[49,53] The impurity peaks around 23° correspond to the presence of $Li_2CO_3/NiCO_3$ as the surface impurity.[54] The tap density of the LNCMO811 is 1.34 g/cm^3. SEM images (Figure 6b,c) indicated that the nanosheet morphology transformed to spherical microparticles after the lithiation process. Energy dispersive X-ray analysis (EDAX) mapping (Figure 6d) verified the homogeneous distribution of all of the transition metals.

Table 1. Lattice Parameter of LNCMO

a (Å)	c (Å)	c/a	volume (Å^3)	$I_{(003)}/I_{(104)}$
2.87	14.2	4.95	101.59	1.7

3.3. Electrochemical Performance. The electrochemical performance of the as-synthesized LNCMO811 was evaluated by fabricating the coin cell, using the active material as the cathode and Li-foil as the anode. The cyclic voltammetric (CV) experiment was performed within the voltage window of 3−4.4 V vs Li/Li$^+$. The presence of multiple redox signatures in the CV profile indicates the phase transitions of the cathode material during the Li$^+$ intercalation/deintercalation process (Figure 7a). Careful analysis of the redox signatures is important to understand the potential cycling-induced phase change in the high-Ni-content NCM, such as NCM811-based cathodes. Three pairs of redox signatures in the cyclic voltammogram correspond to the stepwise phase transition of the cathode material from hexagonal1 (H1) → monoclinic (M) → hexagonal 2 (H2) → hexagonal 3 (H3). The phase transitions are associated with the redox change of the transition-metal ions present in the NCM moiety. The peak at 3.8/3.72 and 4.22/4.18 V corresponds to the Ni^{2+}/Ni^{4+} and Co^{3+}/Co^{4+}, respectively.[55] It is worth mentioning that the transition from H2 to H3, which takes place above the 4.2 V vs Li/Li$^+$, results from the lattice shrinkage in the c direction, leading toward the structural degradation and performance fading.[56]

Hence, an operating potential window of 3.0−4.2 V vs Li/Li$^+$ was selected to perform the rest of the electrochemical experiments. Figure 7b shows the charge−discharge performance of NCM811 at different C rates. The material also shows the specific capacities of 169.5, 163.53, 148.76, and 128.77 mAh g^{-1} at the current rates of 0.1, 0.2, 0.5, and 1C, respectively. The charge−discharge plateau gap was found to be increased with the C-rate, which signifies the higher polarization of the electrode. The rate capability plot (Figure 7c) is generated based on the results of the charge−discharge experiments. It is observed that the material regains ∼99.5% of its initial specific capacity once the current rate was decreased from 1 to 0.1C again. The material shows promising performance in terms of the Coulombic efficiency of ∼100% at all of the current rates. One of the primary issues with the high-Ni-content NCM-based cathodes is their poor cycling

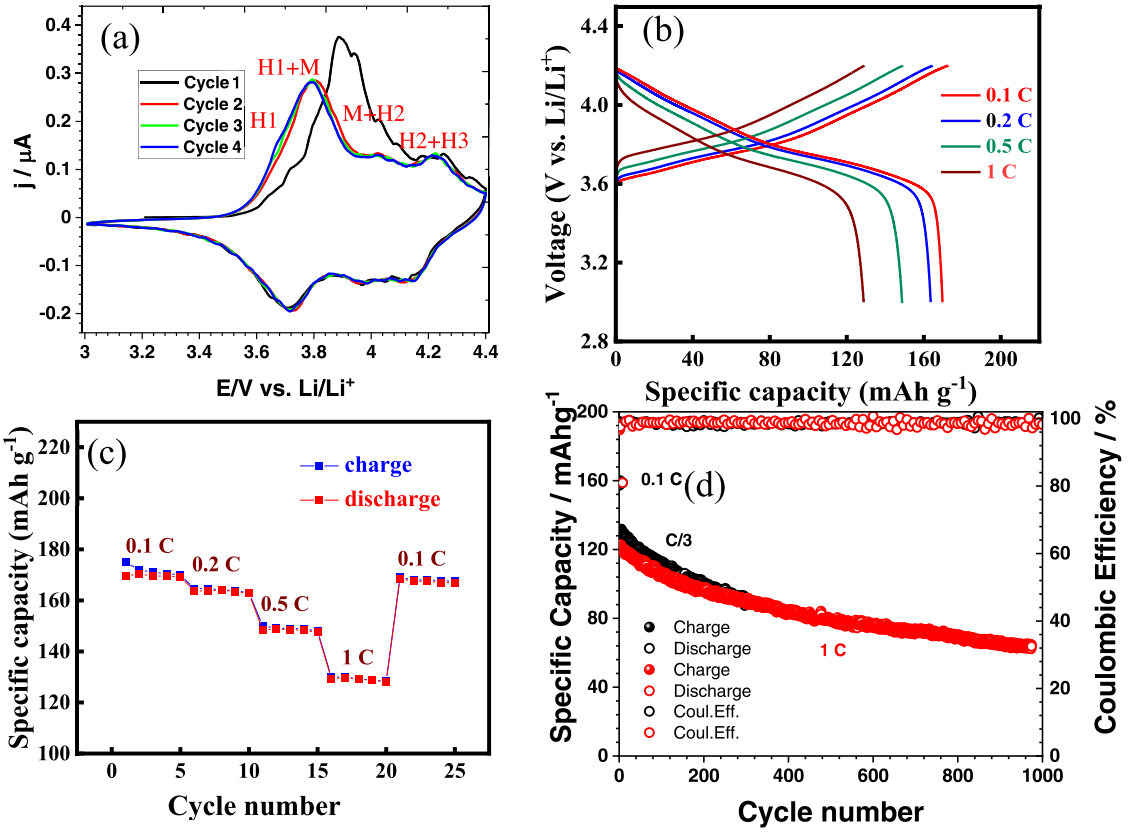

Figure 7. (a) Cyclic voltammetric profile, (b) galvanostatic charge−discharge, (c) rate capability plot, and (d) cycling performance of the NCM811-based coin cell LIB.

https://doi.org/10.1021/acsomega.2c05521
ACS Omega 2022, 7, 42408−42417

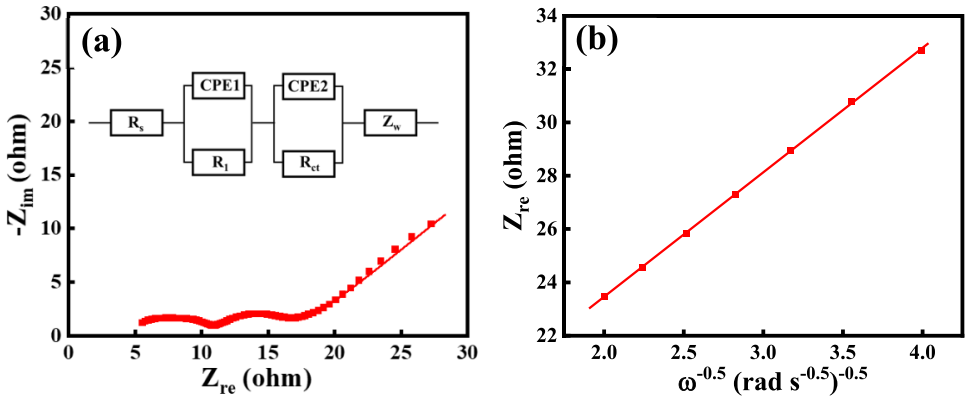

Figure 8. (a) Fitted Nyquist plot and (b) Z_{re} vs $\omega^{-0.5}$ derived from the Warburg region of the Nyquist plot (low-frequency region) of the NCM811-based coin cell LIB. The equivalent circuit is given in the inset of panel (a).

performance due to the higher extent of Ni/Li mixing, mechanical degradation due to phase transition from layered to spinel to rocksalt structure, and microcrack formation.[57] The cycling stability test was performed for 1000 cycles at 1C (Figure 7d), and even at the end of the 1000 consecutive charge−discharge cycles, it shows a capacity retention of ∼66 mAh g^{-1}.

Electrochemical impedance spectroscopy (EIS) was used to evaluate the battery performance in detail. In this case, the EIS analysis was performed within the frequency range of 100 kHz to 10 mHz with an amplitude of 5 mV. The as-obtained Nyquist plot (Figure 8a) contains two semicircles at the higher-frequency range and the Warburg line at the lower-frequency range. To analyze the impedance behavior in detail, the Nyquist plot was fitted, using a suitable equivalent circuit (Figure 6a, inset). The equivalent circuit is made of the following components: (i) solution resistance (R_s); (ii) charge-transfer resistance (R_{ct}); (iii) surface resistance (R_1); (iv) constant phase elements (CPE1 and CPE2); and (v) Warburg impedance (Z_w). The two semicircles at the high-frequency region are associated with one CPE and one resistance component (R_{ct} and R_1) each and thus associated with two different time constants ($\tau = RC$).[58] The Warburg impedance line at the low-frequency region of the impedance plot determines the diffusion behavior of the Li^+ ion in the bulk phase. The Li^+ diffusion coefficient (D_{Li+}) is related to the Warburg component through the following equation[59,60]

$$D = R^2T^2(2A^2n^4F^4C^2\sigma^2)^{-1} \quad (9)$$

where R is the gas constant, T is the absolute temperature, A is the area of the electrode, N is the number of electrons transferred per molecule in the electrochemical reaction, F is the Faraday constant, C is the concentration of Li^+ ions, and σ is the Warburg factor. The Warburg factor (σ) can be calculated from the slope of the $Z_{re} - \omega^{-0.5}$ plot (Figure 8b), using the following relation

$$Z_{re} = R_s + R_{ct} + \sigma\omega^{-0.5} \quad (10)$$

where ω is the angular frequency. The NCM811 shows a diffusion coefficient value of 9.11×10^{-11} cm^2 s^{-1}. The magnitude of the as-calculated Li^+ diffusion coefficient is in accordance with the already reported values for NCM811.[1,44] The fitted impedance data are given in Table 2. The electrochemical performance of NCM811 synthesized by slug flow followed by calcination process is comparable with the reported NCM811 data (Table S2). The primary advantage of the slug flow synthesis platform is that it allows to scale up the production rate without altering the reaction environment inside each slug and hence offers uniformity in particle composition.

Table 2. Fitted Parameters from Impedance Analysis

R_s (Ω)	R_1 (Ω)	R_{ct} (Ω)	D_{Li+} (cm^2 s^{-1})
5.02	4.99	7.12	9.11×10^{-11}

4. CONCLUSIONS

The NCM811 precursor for lithium-ion battery cathode has been produced by combining the three-phase slug flow reactor with the ripening flask for the first time. The batch process was converted into the three-phase slug flow reactor by injecting the starting materials in sequence. The coprecipitation process has been controlled well without fouling by designing the injection of reagents at different locations. The proposed process can be scaled up easily by increasing the operational time. The modeling predicts that a 75% yield of product can be achieved before ripening at an ammonia concentration of 0.5 M and a pH of 10. The lithiated sample from the three-phase slug flow reactor demonstrated a low cation mixing and high tap density (1.34 g/cm^3). The EDX elemental mapping proved that all of the elements are uniformly distributed throughout the material for both the slug flow-produced precursor and the lithiated material. The excellent internal mixing and coprecipitation inside each of the microliter slugs improve the synthesis process. As-synthesized cathodes delivered specific capacities of 169.5, 163.53, 148.76, and 128.77 mAh g^{-1} at current rates of 0.1, 0.2, 0.5, and 1C (200 mAh g^{-1}), respectively, and a cycling performance of 1000 cycles with good capacity retention. This work gives a prominent indication of the wide prospects of successful utilization of the slug flow platform for the production of high-quality battery materials on a commercial scale.

■ ASSOCIATED CONTENT

Supporting Information

The Supporting Information is available free of charge at https://pubs.acs.org/doi/10.1021/acsomega.2c05521.

XRD; equilibrium constants, and comparative table of slug-flow (PDF)

https://doi.org/10.1021/acsomega.2c05521
ACS Omega 2022, 7, 42408−42417

AUTHOR INFORMATION

Corresponding Authors

Mariappan Parans Paranthaman − *Chemical Sciences Division, Oak Ridge National Laboratory, Oak Ridge, Tennessee 37831, United States;* orcid.org/0000-0003-3009-8531; Email: paranthamanm@ornl.gov

Mo Jiang − *Department of Chemical and Life Science Engineering, Virginia Commonwealth University, Richmond, Virginia 23219, United States*; Email: mjiang3@vcu.edu

Authors

Mingyao Mou − *Department of Chemical and Life Science Engineering, Virginia Commonwealth University, Richmond, Virginia 23219, United States*

Arjun Patel − *Department of Chemical and Life Science Engineering, Virginia Commonwealth University, Richmond, Virginia 23219, United States*

Sourav Mallick − *Department of Chemical and Life Science Engineering, Virginia Commonwealth University, Richmond, Virginia 23219, United States*

Bishnu P. Thapaliya − *Chemical Sciences Division, Oak Ridge National Laboratory, Oak Ridge, Tennessee 37831, United States;* orcid.org/0000-0002-1697-0509

Jethrine H. Mugumya − *Department of Chemical and Life Science Engineering, Virginia Commonwealth University, Richmond, Virginia 23219, United States;* orcid.org/0000-0003-4319-4725

Michael L. Rasche − *Department of Chemical and Life Science Engineering, Virginia Commonwealth University, Richmond, Virginia 23219, United States*

Ram B. Gupta − *Department of Chemical and Life Science Engineering, Virginia Commonwealth University, Richmond, Virginia 23219, United States;* orcid.org/0000-0002-4385-0799

Selma Saleh − *Department of Chemical and Life Science Engineering, Virginia Commonwealth University, Richmond, Virginia 23219, United States*

Sophie Kothe − *Department of Chemical and Life Science Engineering, Virginia Commonwealth University, Richmond, Virginia 23219, United States*

Ena Baral − *Department of Chemical and Life Science Engineering, Virginia Commonwealth University, Richmond, Virginia 23219, United States*

Gaind P. Pandey − *Department of Chemical and Life Science Engineering, Virginia Commonwealth University, Richmond, Virginia 23219, United States*

Herman Lopez − *Zenlabs Energy Inc., Fremont, California 94538, United States*

Complete contact information is available at: https://pubs.acs.org/10.1021/acsomega.2c05521

Author Contributions

M.M. and M.J. designed the slug flow process and platform for synthesizing the cathode precursor microparticles. M.M. performed the experiments and characterizations, analyzed the data, and wrote the manuscript. G.P.P. helped with the experimental design and optimize the lithiation parameters. S.M. and A.P. performed the lithiation and battery performance test and wrote the manuscript. S.S., S.K., and E.B. performed experiments. M.L.R. built the mathematical model. J.M. performed the ICP tests. B.P.T. and M.P.P. performed the battery performance test. H.L. helped with the experimental design. R.B.G., M.P.P., and M.J. conceived the idea and supervised the project. All of the authors contributed to the writing and reviewing of the manuscript and approved the final version of the manuscript.

Notes

The authors declare no competing financial interest.

ACKNOWLEDGMENTS

This research was supported by Virginia Commonwealth University, the National Science Foundation (Grant No. CMMI-1940948), and the U.S. Department of Energy, Office of Energy Efficiency and Renewable Energy, Advanced Manufacturing Office (award DE-EE0009110). Research conducted at ORNL was supported by the U.S. Department of Energy, Office of Energy Efficiency and Renewable Energy, Advanced Manufacturing Office. BPT and MPP (battery testing) were supported by the U.S. Department of Energy, Office of Science, Basic Energy Sciences, Materials Sciences and Engineering Division under contract number DEAC05-00OR22725. This manuscript has been authored by UT-Battelle, LLC, under Contract No. DEAC05-00OR22725 with the U.S. Department of Energy. The U.S. Government retains and the publisher, by accepting the article for publication, acknowledges that the U.S. Government retains a nonexclusive, paid-up, irrevocable, worldwide license to publish or reproduce the published form of this manuscript, or allow others to do so, for U.S. Government purposes. The Department of Energy will provide public access to these results of federally sponsored research in accordance with the DOE Public Access Plan (http://energy.gov/downloads/doe-public-access-plan).

REFERENCES

(1) Noh, H.-J.; Youn, S.; Yoon, C. S.; Sun, Y. Comparison of the Structural and Electrochemical Properties of Layered Li-[NixCoyMnz]O2 (x = 1/3, 0.5, 0.6, 0.7, 0.8 and 0.85) Cathode Material for Lithium-Ion Batteries. *J. Power Sources* **2013**, *233*, 121−130.

(2) Schipper, F.; Erickson, E. M.; Erk, C.; Shin, J.-Y.; Chesneau, F. F.; Aurbach, D. Review—Recent Advances and Remaining Challenges for Lithium Ion Battery Cathodes. *J. Electrochem. Soc.* **2017**, *164*, A6220−A6228.

(3) Sun, X.-G.; Jafta, C. J.; Tan, S.; Borisevich, A.; Gupta, R. B.; Paranthaman, M. P. Facile Surface Coatings for Performance Improvement of NMC811 Battery Cathode Material. *J. Electrochem. Soc.* **2022**, *169*, No. 020565.

(4) Wang, G.; Yi, L.; Yu, R.; Wang, X.; Wang, Y.; Liu, Z.; Wu, B.; Liu, M.; Zhang, X.; Yang, X.; Xiong, X.; Liu, M. Li1.2Ni0.13-Co0.13Mn0.54O2 with Controllable Morphology and Size for High Performance Lithium-Ion Batteries. *ACS Appl. Mater. Interfaces* **2017**, *9*, 25358−25368.

(5) Ahmed, S.; Nelson, P. A.; Gallagher, K. G.; Susarla, N.; Dees, D. W. Cost and Energy Demand of Producing Nickel Manganese Cobalt Cathode Material for Lithium Ion Batteries. *J. Power Sources* **2017**, *342*, 733−740.

(6) Demirocak, D. E.; Srinivasan, S. S.; Stefanakos, E. K. A Review on Nanocomposite Materials for Rechargeable Li-Ion Batteries. *Appl. Sci.* **2017**, *7*, No. 731.

(7) Wan, J.; Xie, J.; Mackanic, D. G.; Burke, W.; Bao, Z.; Cui, Y. Status, Promises, and Challenges of Nanocomposite Solid-State Electrolytes for Safe and High Performance Lithium Batteries. *Mater. Today Nano* **2018**, *4*, 1−16.

(8) Shi, Y.; Chen, G.; Chen, Z. Effective Regeneration of LiCoO2 from Spent Lithium-Ion Batteries: A Direct Approach towards High-Performance Active Particles. *Green Chem.* **2018**, *20*, 851−862.

(9) Choi, N. S.; Chen, Z.; Freunberger, S. A.; Ji, X.; Sun, Y. K.; Amine, K.; Yushin, G.; Nazar, L. F.; Cho, J.; Bruce, P. G. Challenges

Facing Lithium Batteries and Electrical Double-Layer Capacitors. *Angew. Chem., Int. Ed.* **2012**, *51*, 9994−10024.
(10) Zhang, Y.; Gao, Z.; Song, N.; He, J.; Li, X. Graphene and Its Derivatives in Lithium−Sulfur Batteries. *Mater. Today Energy* **2018**, *9*, 319−335.
(11) Teki, R.; Datta, M. K.; Krishnan, R.; Parker, T. C.; Lu, T.-M.; Kumta, P. N.; Koratkar, N. Nanostructured Silicon Anodes for Lithium Ion Rechargeable Batteries. *Small* **2009**, *5*, 2236−2242.
(12) Liang, L.; Zhang, W.; Zhao, F.; Denis, D. K.; uz Zaman, F.; Hou, L.; Yuan, C. Surface/Interface Structure Degradation of Ni-Rich Layered Oxide Cathodes toward Lithium-Ion Batteries: Fundamental Mechanisms and Remedying Strategies. *Adv. Mater. Interfaces* **2020**, *7*, No. 1901749.
(13) Zhang, W.; Liang, L.; Zhao, F.; Liu, Y.; Hou, L.; Yuan, C. Ni-Rich LiNi0·8Co0·1Mn0·1O2 Coated with Li-Ion Conductive Li3PO4 as Competitive Cathodes for High-Energy-Density Lithium Ion Batteries. *Electrochim. Acta* **2020**, *340*, No. 135871.
(14) Zhao, F.; Li, X.; Yan, Y.; Su, M.; Liang, L.; Nie, P.; Hou, L.; Chang, L.; Yuan, C. A Three-in-One Engineering Strategy to Achieve LiNi0.8Co0.1Mn0.1O2 Cathodes with Enhanced High-Voltage Cycle Stability and High-Rate Capacities towards Lithium Storage. *J. Power Sources* **2022**, *524*, No. 231035.
(15) Luo, Y.-h.; Wei, H.; Tang, L.; Huang, Y.; Wang, Z.; He, Z.; Yan, C.; Mao, J.; Dai, K.; Zheng, J. Nickel-Rich and Cobalt-Free Layered Oxide Cathode Materials for Lithium Ion Batteries. *Energy Storage Mater.* **2022**, *50*, 274−307.
(16) Wei, J.; Liang, D.; Ji, Y.; Chen, B.; Jiang, C.; Li, X. Enhanced Electrochemical Performance of Cobalt Oxide Layers Coated LiNi0.8Co0.1Mn0.1O2 by Polyvinylpyrrolidone-Assisted Method Cathode for Li-Ion Batteries. *J. Colloid Interface Sci.* **2022**, *616*, 520−531.
(17) Zhang, S. S. Understanding of Performance Degradation of LiNi0.80Co0.10Mn0.10O2 Cathode Material Operating at High Potentials. *J. Energy Chem.* **2020**, *41*, 135−141.
(18) Xiangtao, B.; Liqing, B.; Weidong, Z. Research Progress on Coating and Doping Modification of Nickel Rich Ternary Cathode Materials. *J. Inorg. Mater.* **2020**, *35*, 972−986.
(19) Zheng, S.; Hong, C.; Guan, X.; Xiang, Y.; Liu, X.; Xu, G.-L.; Liu, R.; Zhong, G.; Zheng, F.; Li, Y.; Zhang, X.; Ren, Y.; Chen, Z.; Amine, K.; Yang, Y. Correlation between Long Range and Local Structural Changes in Ni-Rich Layered Materials during Charge and Discharge Process. *J. Power Sources* **2019**, *412*, 336−343.
(20) Shim, J.-H.; Im, J.-S.; Kang, H.; Cho, N.; Kim, Y.-M.; Lee, S. Implications of Cation-Disordered Grain Boundaries on the Electrochemical Performance of the LiNi0.5Co0.2Mn0.3O2 Cathode Material for Lithium Ion Batteries. *J. Mater. Chem. A* **2018**, *6*, 16111−16120.
(21) Zhang, J.; Zhang, J.; Ou, X.; Wang, C.; Peng, C.; Zhang, B. Enhancing High-Voltage Performance of Ni-Rich Cathode by Surface Modification of Self-Assembled NASICON Fast Ionic Conductor LiZr2(PO4)3. *ACS Appl. Mater. Interfaces* **2019**, *11*, 15507−15516.
(22) Wei, H.-x.; Tang, L.; Huang, Y.; Wang, Z.; Luo, Y.; He, Z.; Yan, C.; Mao, J.; Dai, K.; Zheng, J. Comprehensive Understanding of Li/Ni Intermixing in Layered Transition Metal Oxides. *Mater. Today* **2021**, *51*, 365−392.
(23) Lv, Y.; Huang, S.; Zhao, Y.; Roy, S.; Lu, X.; Hou, Y.; Zhang, J. A Review of Nickel-Rich Layered Oxide Cathodes: Synthetic Strategies, Structural Characteristics, Failure Mechanism, Improvement Approaches and Prospects. *Appl. Energy* **2022**, *305*, No. 117849.
(24) Su, Y.; Chen, G.; Chen, L.; Lu, Y.; Zhang, Q.; Lv, Z.; Li, C.; Li, L.; Liu, N.; Tan, G.; Bao, L.; Chen, S.; Wu, F. High-Rate Structure-Gradient Ni-Rich Cathode Material for Lithium-Ion Batteries. *ACS Appl. Mater. Interfaces* **2019**, *11*, 36697−36704.
(25) Fan, X.; Hu, G.; Zhang, B.; Ou, X.; Zhang, J.; Zhao, W.; Jia, H.; Zou, L.; Li, P.; Yang, Y. Crack-Free Single-Crystalline Ni-Rich Layered NCM Cathode Enable Superior Cycling Performance of Lithium-Ion Batteries. *Nano Energy* **2020**, *70*, No. 104450.
(26) Dong, H.; Wang, A.; Koenig, G. M. Role of Coprecipitation and Calcination of Precursors on Phase Homogeneity and Electrochemical Properties of Battery Active Materials. *Powder Technol.* **2018**, *335*, 137−146.
(27) Taniguchi, I.; Fukuda, N.; Konarova, M. Synthesis of Spherical LiMn2O4 Microparticles by a Combination of Spray Pyrolysis and Drying Method. *Powder Technol.* **2008**, *181*, 228−236.
(28) Amine, K.; Tukamoto, H.; Yasuda, H.; Fujita, Y. Preparation and electrochemical investigation of LiMn2-xMexO4 (Me: Ni, Fe, and x=0.5, 1) cathode materials for secondary lithium batteries. *J. Power Sources* **1997**, *68*, 604−608.
(29) Xu, L.; Zhou, F.; Liu, B.; Zhou, H.; Zhang, Q.; Kong, J.; Wang, Q. Progress in Preparation and Modification of $LiNi_{0.6}Mn_{0.2}Co_{0.2}O_2$ Cathode Material for High Energy Density Li-Ion Batteries. *Int. J. Electrochem.* **2018**, *2018*, No. 6930386.
(30) Liu, Y. C.; Dunn, D.; Lipari, M.; Barton, A.; Firth, P.; Speed, J.; Wood, D.; Nagy, Z. K. A Comparative Study of Continuous Operation between a Dynamic Baffle Crystallizer and a Stirred Tank Crystallizer. *Chem. Eng. J.* **2019**, *367*, 278−294.
(31) Coley, C. W.; Imbrogno, J.; Mo, Y.; Thomas, D. A.; Jensen, K. F.Flow Chemistry System Design and Automation. In *Science of Synthesis*2018; Vol. *2018*, pp 3−50.
(32) Nagy, Z. K.; Braatz, R. D. Advances and New Directions in Crystallization Control. *Annu. Rev. Chem. Biomol. Eng.* **2012**, *3*, 55−75.
(33) Zhang, D.; Xu, S.; Du, S.; Wang, J.; Gong, J. Progress of Pharmaceutical Continuous Crystallization. *Engineering* **2017**, *3*, 354−364.
(34) Xiao, X.; Duan, X.; Song, Z.; Deng, X.; Deng, W.; Hou, H.; Zheng, R.; Zou, G.; Ji, X. High-Throughput Production of Cheap Mineral-Based Heterostructures for High Power Sodium Ion Capacitors. *Adv. Funct. Mater.* **2022**, *32*, No. 2110476.
(35) Gary, J. H.; Handwerk, J. H.; Kaiser, M. J.; Geddes, D.*Petroleum Refining: Technology and Economics*, 5th ed.; CRC Press, 2007.
(36) Narchi, I.; Vial, C.; Djelveh, G. Effect of Protein−Polysaccharide Mixtures on the Continuous Manufacturing of Foamed Food Products. *Food Hydrocolloids* **2009**, *23*, 188−201.
(37) Mascia, S.; Heider, P. L.; Zhang, H.; Lakerveld, R.; Benyahia, B.; Barton, P. I.; Braatz, R. D.; Cooney, C. L.; Evans, J. M. B.; Jamison, T. F.; Jensen, K. F.; Myerson, A. S.; Trout, B. L. End-to-End Continuous Manufacturing of Pharmaceuticals: Integrated Synthesis, Purification, and Final Dosage Formation. *Angew. Chem., Int. Ed.* **2013**, *52*, 12359−12363.
(38) Lee, S. L.; O'Connor, T. F.; Yang, X.; Cruz, C. N.; Chatterjee, S.; Madurawe, R. D.; Moore, C. M. V.; Yu, L. X.; Woodcock, J. Modernizing Pharmaceutical Manufacturing: From Batch to Continuous Production. *J. Pharm. Innovation* **2015**, *10*, 191−199.
(39) Croughan, M. S.; Konstantinov, K. B.; Cooney, C. The Future of Industrial Bioprocessing: Batch or Continuous? *Biotechnol. Bioeng.* **2015**, *112*, 648−651.
(40) Jiang, M.; Zhu, Z.; Jimenez, E.; Papageorgiou, C. D.; Waetzig, J.; Hardy, A.; Langston, M.; Braatz, R. D. Continuous-Flow Tubular Crystallization in Slugs Spontaneously Induced by Hydrodynamics. *Cryst. Growth Des.* **2014**, *14*, 851−860.
(41) Mendorf, M.; Nachtrodt, H.; Mescher, A.; Ghaini, A.; Agar, D. W. Design and Control Techniques for the Numbering-up of Capillary Microreactors with Uniform Multiphase Flow Distribution. *Ind. Eng. Chem. Res.* **2010**, *49*, 10908−10916.
(42) Nightingale, A. M.; Phillips, T. W.; Bannock, J. H.; De Mello, J. C. Controlled Multistep Synthesis in a Three-Phase Droplet Reactor. *Nat. Commun.* **2014**, *5*, No. 3777.
(43) Jongen, N.; Donnet, M.; Bowen, P.; Lemaître, J.; Hofmann, H.; Schenk, R.; Hofmann, C.; Aoun-Habbache, M.; Guillemet-Fritsch, S.; Sarrias, J.; Rousset, A.; Viviani, M.; Buscaglia, M. T.; Buscaglia, V.; Nanni, P.; Testino, A.; Herguijuela, J. R. Development of a Continuous Segmented Flow Tubular Reactor and the "Scale-out" Concept − In Search of Perfect Powders. *Chem. Eng. Technol.* **2003**, *26*, 303−305.
(44) Wei, Y.; Zheng, J.; Cui, S.; Song, X.; Su, Y.; Deng, W.; Wu, Z.; Wang, X.; Wang, W.; Rao, M.; Lin, Y.; Wang, C.; Amine, K.; Pan, F.

https://doi.org/10.1021/acsomega.2c05521
ACS Omega 2022, 7, 42408−42417

Kinetics Tuning of Li-Ion Diffusion in Layered Li(NixMnyCoz)O2. *J. Am. Chem. Soc.* **2015**, *137*, 8364−8367.
(45) Shen, Y.; Wu, Y.; Xue, H.; Wang, S.; Yin, D.; Wang, L.; Cheng, Y. Insight into the Coprecipitation-Controlled Crystallization Reaction for Preparing Lithium-Layered Oxide Cathodes. *ACS Appl. Mater. Interfaces* **2021**, *13*, 717−726.
(46) Hua, W.; Liu, W.; Chen, M.; Indris, S.; Zheng, Z.; Guo, X.; Bruns, M.; Wu, T. H.; Chen, Y.; Zhong, B.; Chou, S.; Kang, Y. M.; Ehrenberg, H. Unravelling the Growth Mechanism of Hierarchically Structured Ni1/3Co1/3Mn1/3(OH)2 and Their Application as Precursors for High-Power Cathode Materials. *Electrochim. Acta* **2017**, *232*, 123−131.
(47) Han, Y.; Shan, X.; Zhu, G.; Wang, Y.; Qu, Q.; Zheng, H. Hierarchically Assembled LiNi0.8Co0.1Mn0.1O2 Secondary Particles with High Exposure of {010} Plane Synthesized via Co-Precipitation Method. *Electrochim. Acta* **2020**, *329*, No. 135057.
(48) Mou, M.; Li, H.; Yang, B.-S.; Jiang, M. Continuous Generation of Millimeter-Sized Glycine Crystals in Non-Seeded Millifluidic Slug Flow. *Crystals* **2019**, *9*, No. 412.
(49) Xue, L.; Li, Y.; Han, Q.; Su, Q.; Chen, Y.; Li, J.; Lei, T.; Chen, Y.; Chen, J. Effect of High-Temperature Crystallization on the Electrochemical Properties of LiNi0.5Co0.2Mn0.3O2 Synthesized from a Lithiated Transition Metal Oxide Precursor. *Ionics* **2018**, *24*, 2957−2963.
(50) Dong, H.; Koenig, G. M. A Review on Synthesis and Engineering of Crystal Precursors Produced: Via Coprecipitation for Multicomponent Lithium-Ion Battery Cathode Materials. *CrystEngComm* **2020**, *22*, 1514−1530.
(51) Park, H.; Park, H.; Song, K.; Song, S. H.; Kang, S.; Ko, K. H.; Eum, D.; Jeon, Y.; Kim, J.; Seong, W. M.; Kim, H.; Park, J.; Kang, K. In Situ Multiscale Probing of the Synthesis of a Ni-Rich Layered Oxide Cathode Reveals Reaction Heterogeneity Driven by Competing Kinetic Pathways. *Nat. Chem.* **2022**, *14*, 614−622.
(52) Zhu, J.; Vo, T.; Li, D.; Lu, R.; Kinsinger, N. M.; Xiong, L.; Yan, Y.; Kisailus, D. Crystal Growth of Li[Ni1/3Co1/3Mn1/3]O2 as a Cathode Material for High-Performance Lithium Ion Batteries. *Cryst. Growth Des.* **2012**, *12*, 1118−1123.
(53) Nisa, S. S.; Rahmawati, M.; Yudha, C. S.; Nilasary, H.; Nursukatmo, H.; Oktaviano, H. S.; Muzayanha, S. U.; Purwanto, A. Fast Approach to Obtain Layered Transition-Metal Cathode Material for Rechargeable Batteries. *Batteries* **2022**, *8*, No. 4.
(54) Fang, Z.; Confer, M. P.; Wang, Y.; Wang, Q.; Kunz, M. R.; Dufek, E. J.; Liaw, B.; Klein, T. M.; Dixon, D. A.; Fushimi, R. Formation of Surface Impurities on Lithium−Nickel−Manganese−Cobalt Oxides in the Presence of CO2 and H2O. *J. Am. Chem. Soc.* **2021**, *143*, 10261−10274.
(55) Roitzheim, C.; Kuo, L. Y.; Sohn, Y. J.; Finsterbusch, M.; Möller, S.; Sebold, D.; Valencia, H.; Meledina, M.; Mayer, J.; Breuer, U.; Kaghazchi, P.; Guillon, O.; Fattakhova-Rohlfing, D. Boron in Ni-Rich NCM811 Cathode Material: Impact on Atomic and Microscale Properties. *ACS Appl. Energy Mater.* **2022**, *5*, 524−538.
(56) Ryu, H. H.; Park, K. J.; Yoon, C. S.; Sun, Y. K. Capacity Fading of Ni-Rich Li[NixCoyMn1-x-y]O2 ($0.6 \leq x \leq 0.95$) Cathodes for High-Energy-Density Lithium-Ion Batteries: Bulk or Surface Degradation? *Chem. Mater.* **2018**, *30*, 1155−1163.
(57) Chen, S.; Zhang, X.; Xia, M.; Wei, K.; Zhang, L.; Zhang, X.; Cui, Y.; Shu, J. Issues and Challenges of Layered Lithium Nickel Cobalt Manganese Oxides for Lithium-Ion Batteries. *J. Electroanal. Chem.* **2021**, *895*, No. 115412.
(58) Cheng, C.; Drummond, R.; Duncan, S. R.; Grant, P. S. Micro-Scale Graded Electrodes for Improved Dynamic and Cycling Performance of Li-Ion Batteries. *J. Power Sources* **2019**, *413*, 59−67.
(59) Zheng, J.-c.; Yang, Z.; He, Z.-j.; Tong, H.; Yu, W.-j.; Zhang, J.-f. In Situ Formed LiNi0.8Co0.15Al0.05O2@Li4SiO4 Composite Cathode Material with High Rate Capability and Long Cycling Stability for Lithium-Ion Batteries. *Nano Energy* **2018**, *53*, 613−621.
(60) Bard, A. J.; Faukner, L. R.*Electrochemical Methods: Fundamentals and Applications*; John Wiley & Sons, 1980.

https://doi.org/10.1021/acsomega.2c05521
ACS Omega 2022, 7, 42408−42417